Indian Journal of Pure & Applied Physics
Vol. 62, May 2024, pp. 372-387
DOI: 10.56042/ijpap.v62i5.6177

Study on Thermal Transport and Flow Characterization of TiO_2-SiO_2 Mixture Slippery Nanoflow Under Energy Generation: Keller Box Simulation

B Vinothkumar & T Poornima*

Department of Mathematics, School of Advanced Sciences, Vellore Institute of Technology, Vellore, Tamil Nadu 632 014, India

Received 12 October 2023; accepted 1 January 2024

An impactful rheological fluid model (Casson) has taken for study. The influence of nanoparticles mixture $(SiO_2), (Al_2O_3), (TiO_2)$ suspended in water based slippery radiative nanoflow around a porous cylinder has investigated in the presence of non-uniform energy generation or absorption. A suitable Casson rheological mathematical model has been developed as set of partial differential equations and transformed to system of ordinary differential equation under self-similarity transformations. Then, the final system has cracked numerically employing Keller box method, coded with MATLAB. The numerical solutions for Nusselt number, surface friction coefficient, momentum and energy profiles have portrayed and tabulated. Streamlines have drawn for analysing the amount of energy flow characterisation. A three-way comparison has done based on number of nanoparticles added to the base flow. The study has revealed that among three different models of nanoflow (simple nanoflow, hybrid nanoflow, ternary nanoflow), hybrid nanoflow has shown the best heat transmission rate and momentum flow rate. In hybrid nanofluids, an increasing heat transfer rate and surface friction coefficient has noticed for enhancing energy generation parameter. Presence of nano-silica particles have enhanced the high reflectivity of radiation. The oxide nanoclusters and their composite synthesis helps in hydrophobic applications such as in powdering and coating processes. Titania and Silica combination has a superiority in removing heat outside from the surface and this quality has a very good application in cosmetics especially in the sunscreen lotions.

Keywords: Ternary hybrid nanofluid; Casson model; Keller–Box numerical method; Heat transfer; Non-uniform heat production; Magnetic field

1 Introduction

The development of the twenty-first century strongly advocated the development of a new, more efficient thermal energy source to address the energy crisis and, as a result, boost global industrial development. Energy has a crucial and fundamental function in heavy industries and technical processes. Applications for the movement of boundary layers and heat transfer include the drawing of polymer sheets, the extrusion of metals from dies, and the cooling of metallic plates in showers, among other things. The fluids aptitude for heat conduction and their availability makes them typically utilised for cooling purposes.

The growth of industries led to an increase in the amount of dust, sulphur oxides, and manufacturing gases that pollute the air. As a result, environmental challenges like global warming are becoming major world problems. Along with industrial boilers and electricity generation plants, vehicle movement also contributes to pollution. Nitrogen oxides, which are dangerous air pollutants, are produced by these sources. Due to an increase in the use of automobiles, nitrogen oxide emissions have recently reached hazardous levels in major cities.

The significance of titanium dioxide in photocatalytic applications. Fujishima *et al.*[1] studied the semiconductor electrode which undergoes electrochemical photolysis of water. Ali *et al.*[2] investigated the porous anatase (TiO_2) sol-gel preparation goes through a peptidization process. Hulteen *et al.*[3] demonstrated an all-purpose template-based technique for making nanomaterials. Ming *et al.*[4] experimented the preparation of (TiO_2) nanotubes and nanorods in a soul-gel template. Seo *et al.*[5] discussed the making a TiO2 powder using nanotubes. Fabricating (TiO_2) materials with high specific surface areas results in high photo catalysis. Choi *et al.*[6] used nanoparticles to improve the heat transfer properties of fluids.

Enhancing the qualities of a single molecule that has either superior better heat conductivity or rheological characteristics is the idea behind the creation of nanofluid composites. The heat

*Corresponding author: (E-mail: poornima.t@vit.ac.in)

conductivity and rheological properties of the generated nanofluid is improved by framing a composite nanofluid. By putting the proper nanoparticle mixture, this is ensured. As a result, introducing tiny particles with various thermal or rheological characteristics improves the nanofluid overall functionality and makes it more stable and efficient. For example, aluminium oxide (Al_2O_3) has moderate thermal conductivity yet exhibits notable chemical inertness and stability. In contrast, materials with increased thermal conductivity, instability, and chemical reactivity include aluminium, silver, copper, and other similar materials. As a result, hybrid nanofluids are created when these nanoparticles with various physical and chemical interactions are combined. They have uses in the pharmaceutical sector, nuclear safety, cooling electronic heaters, *etc*.

Wang *et al*.[7] examined the computational analysis of ternary radiative hybrid Casson nano liquid using a rotating cone in Non-Darcian State. Farooq *et al*.[8] numerically studied radiative hybrid nanofluid under stretched surface susceptible to entropy formation. Awwad *et al*.[9] studied the melting heat exchange in bio-convection nanoflow restricted by a symmetrical cylindrical channel with thermal conductivity and swim microbes. Kavafian *et al*.[10] analysed the Brinkman-viscoelastic fluid flowing in a boundary layer of free convection over a vertical cylinder with variable wall temperatures. Ahmad *et al*.[11] have examined radiant bidirectional flow of magnetised hybrid nanofluid. Jamshed *et al*.[12] investigated the thermal properties and entropy optimisation of Cu-methanol Williamson nanofluid via a solar collector using experimental data and TDDFT materials simulation. Chandel *et al*.[13] investigated non-Newtonian nanofluid boundary layer flows over stretching surfaces. Alwawi*et al*.[14] investigated the analysis of the MHD effect on the heat transport of an ethylene glycol-based Casson nanofluid inside a horizontal circular cylinder. Furthermore, numerous investigators have persisted to investigate the process of heat transfer properties of hybrid nanofluids. Kuttan*et al*.[15] discussed the variable viscosity effect on the Marangoni turbulent boundary layer flow of a nanofluid with mixing convection. Abu-Nada *et al*.[16] discussed the variable viscosity and thermal conductivity of an Al2O3-water nanofluid on heat transfer improvement in natural convection. Puneeth *et al*.[17] studied the mixed nanofluid that radiates bioconvects through a tiny needle inserted into the context of a chemical that is heterogeneous and homogenous process.

Heat loses or heat gain in a fluid flow process occurs frequently. It is an inevitable factor when we study energy and species transfer system in a boundary layer theory. Quite good examples of these situations are in building designs, in computers, the CPU, electronic circuits, *etc*. This generation concept is to enhance the fluid conductivity whilst the other (absorption) reduces fluid energy. This term is inevitable when there finds a huge temperature difference and because of this property, energy generation/absorption has greater importance in MHD flows. Fewer applications are in functioning of brain i.e., in neurobiology, magnetized employment of energy generation/absorption has a crucial role. These applications were well discussed by the researchers in their early works[18–20]. Konda *et al*.[21] explored on variable heat sink/source on non-Newtonian fluid. Jyotshna *et al*.[22] extended the same effect over gallium nitride nanoparticles base Williamson flow. Song *et al*.[23] investigated the same effects on stretched cylinder. Swain *et al*.[24] done the same investigation in a porous medium.Shahzad *et al*.[25] investigated the convergence rate of the second order ternary nanofluids, under Hall impact and electromagnetic force across a rotating disc. Oweniid *et al*.[26] investigated the entropy study on a ternary intermixture Hall effect and electromagnetic nanofluid flow models radiation impacts. Islam *et al*.[27] had explored the electro-osmotic flow in blood-based ternary $(TiO_2 - Al_2O_3 - SiO_2)$ Sutterby nanomaterials with bio-active mixers. Manjunatha *et al*.[28] delineated the convective heat exchange ternary nanofluid passing through a stretched sheet. Wang *et al*.[29]considered the impact of Cr_2O_3 on the density and shape of $(CaO - MgO - Al_2O_3 - SiO_2)$ lag (or glass). Sohail *et al*.[30] analysed the ternary hybrid nanoparticles for thermal increase in pseudoplastic liquid through porous stretching sheet. Kalantari *et al*.[31] investigated the use of a $(Cu, Fe_2O_4/H_2O)$ nanofluid to increase the thermal performance of a turbulence cross-flow exchanger for heat circumstances. Zhao *et al*.[32] investigate the Corundum abrasive microstructure and grain formation mechanism with $(Al_2O_3 - TiO_2 - SiO_2)$ composite additions.

The researchers were encouraged to create the present nanofluid idea for boosting heat transfer due to the significant need in the case of a cooling

substance. Three types of nanoparticles with distinct physical and chemical properties have been suspended called trihybrid nanofluid. For example, when treated with sulfuric acid, (TiO_2) produces acid centres with high acid strength and forms a covalent surface sulfatase such as, this research is an effort to create a coolant capable of cooling the appliances. Thus, the supporting ingredients (SiO_2) and (Al_2O_3) are employed to make such a coolant fluid. In support based on the experimental findings, this research presents a theoretical model for ternary hybrid nanofluid under partial and thermal slip under non-symmetric energy past a circular cylinder.

2 Model of mathematical flow

Consider the time independent, laminar, two-dimensional in nature viscous, incompressible, buoyancy-driven convective transfer of heat flow across a horizontal permeable circular cylinder contained a non-Newtonian fluid of Casson type.

$$\tau_{ij} = \begin{cases} e_{ij}\left(\mu_B + \frac{p_y}{\sqrt{2\pi}}\right) 2\,,\ \pi \geq \pi_c \\ e_{ij}\left(\mu_B + \frac{p_y}{\sqrt{2\pi_c}}\right) 2\,,\ \pi < \pi_c \end{cases} \quad \ldots (1)$$

Figure 1 depicts the flow model and mechanical coordinate system. The *x*-axis is calculated around the radius of the cylinder that is horizontally measured from its lowest point, and the direction of the *y*-axis is measured normal to the outermost layer using the letter '*a*' designating the horizontal dimension of a cylinder's diameter. The angle between the *y*-axis and the vertical $(0 \leq \Phi \leq \pi)$ is $(x/a = \Phi)$ The downward force of *g*, or gravitational acceleration. Initially, the horizontal cylinder and the fluid inside both are held at the same temperature. They are instantly increased to a temperature $(T_\infty < T_w)$ above the fluid ambient temperature, which stays constant. In accordance with the approach of Prasad *et al*.[33] the following are the model for conservation is taken:

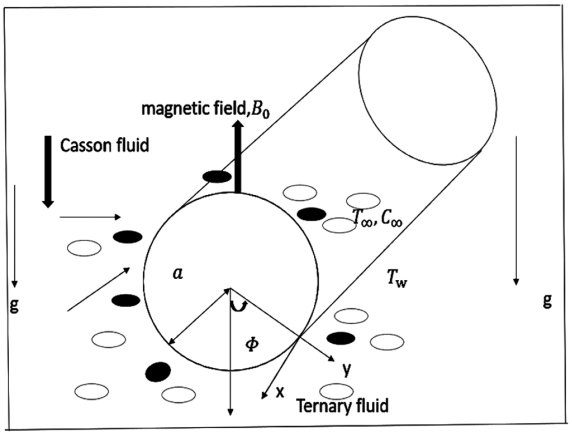

Fig. 1 — Geometry of the problem.

$$\frac{\partial u}{\partial x} + \frac{\partial v}{\partial y} = 0 \quad \ldots(2)$$

$$u\,u_x + v\,u_y = \nu_{thnf}\left(1+\frac{1}{Ca}\right)\frac{\partial^2 u}{\partial y^2} + \frac{\sigma_{thnf}}{\rho_{thnf}} B_0^2\,u + \sin\left(\frac{x}{a}\right) g\Lambda(T-T_\infty) \quad \ldots(3)$$

$$u\,T_x + v\,T_y = k_{thnf}\frac{\partial^2 T}{\partial y^2} + \frac{q'''}{\rho c_p} \quad \ldots(4)$$

where:

$$q''' = \frac{k\,u_w}{xv}\left(A^*(T_W - T_\infty)f' + B^*(T-T_\infty)\right) \quad \ldots(5)$$

The following are the boundary conditions of the cylinder border of the boundary layer regime (free stream) Ramachandra *et al*.[33].

$$y = 0\,;\ \frac{\partial u}{\partial y}\left(1+\frac{1}{Ca}\right)N_0 = u,\quad v = -V_w\,,$$
$$T = K_0\left(k_{thnf}\right)\frac{\partial T}{\partial y} + T_w \quad at\ \ y = 0$$
$$y \to \infty\ ;\ u \to 0,\ \ T \to T_\infty \quad \ldots(6)$$

Because the flow function ψ is determined by $u = \frac{\partial \psi}{\partial y}$ & $v = -\frac{\partial \psi}{\partial x}$ The model for continuous (2) is immediately met. The following nondimensional quantities are added to formulate dimensionless governing equations and boundaries.

$$a = \frac{x}{\xi}\,,\ \eta = \frac{y}{a}(Gr)^{1/4},\ f(\xi,\eta) = \frac{\psi}{\nu\,\xi\,(Gr)^{1/4}},\ \alpha = \frac{\nu}{\mathrm{Pr}},$$
$$\theta(\xi,\eta) = \frac{T-T_\infty}{T_W-T_\infty},\ Gr = \frac{g\Lambda(T_W-T_\infty)\,a^3}{\nu^2},\ Ca = \frac{\sqrt{2\pi_c}}{p_y}\mu_B. \quad \ldots(7)$$

Considering Eq. (7), Eqs. (2) to (4) are reduced to the coupled, nonlinear, domain-specific dimensionless partial differential equations for energy as well as momentum.

$$\xi\left[f'\frac{\partial f'}{\partial \xi} - f''\frac{\partial f}{\partial \xi}\right] = \left(1+\frac{1}{Ca}\right)f'''\left(\frac{\mu_{thnf}}{\mu_f}\right) + \left(\frac{\rho_{thnf}}{\rho_f}\right)(f')^2\left(\frac{\rho_{thnf}}{\rho_f}\right)f\,f'' + \frac{\sin\xi}{\xi}\,\theta + \left(\frac{\sigma_{thnf}}{\sigma_f}\right)M\,f' \quad \ldots(8)$$

$$\frac{1}{\mathrm{Pr}}\left(\frac{k_{thnf}}{k_f}\right)\theta'' + f\,\theta' + M^* f' + N^*\theta = \xi\left[f'\frac{\partial \theta}{\partial \xi} - \frac{\partial f}{\partial \xi}\theta'\right] \quad \ldots(9)$$

Here $M^* = \frac{Ak(Gr)^{1/2}}{g\Lambda(T_W-T_\infty)}$, $N^* = \frac{Bk(Gr)^{1/2}}{g\Lambda(T_W-T_\infty)}$

The boundary conditions are dimensionless altered as:

$$\text{At } \eta = 0,\ S=f,\ f' = f''(0)\ S_F\left(1+\frac{1}{Ca}\right),\theta = \theta'(0)\ S_T\left(\frac{k_t}{k_f}\right)+1.0$$

$$\text{As } \eta\to\infty\ ,\quad \theta\to 0,\quad f'\to 0, \qquad ...(10)$$

Two terms related to engineering are the skin-friction coefficient and the number calculated by Nusselt. Designing those parameters of physical importance.

$$\frac{1}{2}\,Cf\,Gr^{-3/4} = \left(1.0+\frac{1}{Ca}\right)\frac{\mu_{thnf}}{\mu_f}\,\xi f''(0) \qquad ...(11)$$

$$Nu\ Gr^{-1/4} = -\frac{k_{thnf}}{k_f}\ \theta'(0) \qquad ...(12)$$

Thermophysical as well as rheological properties (Manjunatha S *et al.*[28])

The thermophysical characteristics of (H_2O, TiO_2, SiO_2) and (Al_2O_3) Tri hybrid nanofluid are.

(1). Density

$$\rho_{thnf} = (1-\phi_1)\left\{(1-\phi_2)\left[(1-\phi_3)\rho_f + \phi_3\rho_3\right] + \phi_2\rho_2\right\} + \phi_1\rho_1$$

(2). Viscosity

$$\mu_{thnf} = \frac{\mu_f}{(1-\phi_1)^{2.5}\ (1-\phi_2)^{2.5}\ (1-\phi_3)^{2.5}}$$

(3). Thermal conductivity

$$\frac{k_{thnf}}{k_{hnf}} = \frac{k_1+2k_{hnf}-2\phi_1(k_{hnf}-k_1)}{k_1+2k_{hnf}+\phi_1(k_{hnf}-k_1)}$$

Where:

$$\frac{k_{hnf}}{k_{nf}} = \frac{k_2+2k_{nf}-2\,\phi_2(k_{nf}-k_2)}{k_2+2k_{nf}+\phi_2(k_{nf}-k_2)}$$

$$\frac{k_{nf}}{k_f} = \frac{k_3+2k_f-2\,\phi_3(k_f-k_3)}{k_3+2k_f+\phi_3\,(k_f-k_3)}$$

(4). Electrical conductivity

$$\frac{\sigma_{thnf}}{\sigma_{hnf}} = \frac{(1+2\phi_1)\ \sigma_1 + (1-2\phi_1)\ \sigma_{hnf}}{(1-\phi_1)\ \sigma_1 + (1+\phi_1)\ \sigma_{hnf}}$$

Where:

$$\frac{\sigma_{hnf}}{\sigma_{nf}} = \frac{(1+2\phi_2)\ \sigma_2 + (1-2\phi_2)\ \sigma_{nf}}{(1-\phi_2)\ \sigma_2 + (1+\phi_2)\ \sigma_{nf}}$$

$$\frac{\sigma_{nf}}{\sigma_f} = \frac{(1+2\phi_3)\ \sigma_3 + (1-2\phi_3)\ \sigma_f}{(1-\phi_3)\ \sigma_3 + (1+\phi_3)\ \sigma_f}$$

3 KBM (numerical finite difference solution)

The Keller box, an implicit finite difference scheme is a versatile tool for solving parabolic partial differential equations. It's flexibility, accuracy, unconditional stability and easy implementation makes it as a good choice for a wide range of complex geometries. This approach was introduced by Cebeci and Bradshaw[34]. Following the mathematical modelling of the actual method, the next step is to solve the foresaid. We have opted for Keller-Box approach (KBM), a hidden finite differences methodology, for the computational solution of the modelled equations since it combines second-degree validity with the ability of step size adaptation. Since its quicker convergence rate relative to conventional numerical techniques, this approach is best suited for solving boundary layer flow problems (RK method, BVP4c and the shooting technique). Using this approach, higher-order PDEs are reduced to first-order PDEs, which are then transformed by central difference formulae. The decomposition of LU technique is used to solve the matrix-vector form of transformed solutions. The material domain $[0,\infty)$ is used throughout the computation procedure is condensed to the limited area $[\eta_0,\eta_\infty]$ by altering $\eta_0=0, \eta_\infty=20, \eta_p=1000, h=\frac{\eta_\infty-\eta_0}{\eta_p}$ to establish the initial approximations of the computerised solution, and subsequently increasing the total amount of points on the grid by decreasing the step size (h) to attain the necessary precision, $i.e.\varepsilon^{-6}$. A process diagram (Fig. 2) depicts the whole explanation of the Keller-Box simulation/numerical code.

The implicit finite difference technique (Keller box) is used to assess the present modelled undefined nonlinear PDEs (Eqs. 2-4) given the appropriate boundary conditions (Eq. 6). The KBM is discovered to be unconditionally stable and to have second order precision. This technique yields the following solution steps:

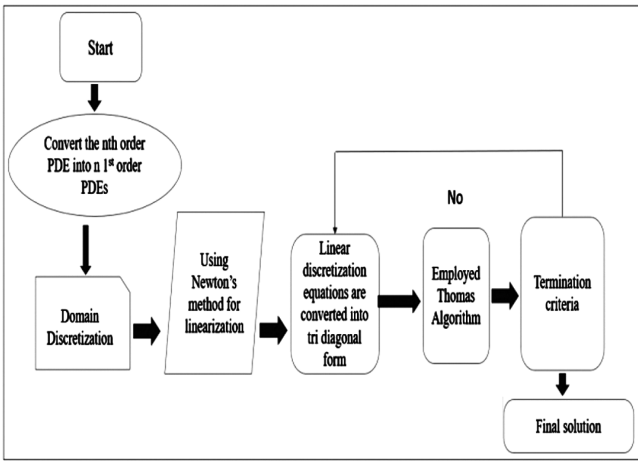

Fig. 2 — Computer-assisted solution using net rectangle mesh and the Keller box element.

Step 1: The Nth order partial differential equation system reduced to N first-order equations.

We add the most recent set of variables listed below to convert higher-order PDEs to first-order PDEs: $p_1(\xi,\eta), p_2(\xi,\eta), p_3(\xi,\eta), p_4(\xi,\eta), p_5(\xi,\eta)$

$$f = f,\ f' = p_1,\ p_1{}' = p_2, \theta = p_3,\ p_3{}' = p_4,\ p_4{}' = p_5 \quad \ldots(13)$$

$$\frac{1}{\Pr}\ (p_4{}')\ \left(\frac{k_t}{k_f}\right) + f(p_4) + A^*(p_1) + B^*(P_3) = \xi\left[p_1\frac{\partial p_3}{\partial \xi} - p_4\frac{\partial f}{\partial \xi}\right] \quad \ldots(15)$$

$$\left(1+\frac{1}{Ca}\right)\ p_2{}'\left(\frac{\mu_{thnf}}{\mu_f}\right) + \left(\frac{\rho_{thnf}}{\rho_f}\right)(f p_2) - \left(\frac{\rho_{thnf}}{\rho_f}\right)(p_1)^2 + \frac{\sin\xi}{\xi}(p_3) + \left(\frac{\sigma_{thnf}}{\sigma_f}\right) M(p_1) = \xi\left[\ p_1\frac{\partial p_1}{\partial \xi} - p_2\frac{\partial f}{\partial \xi}\ \right] \quad \ldots(14)$$

Boundary condition becomes

$$\eta = 0: p_1 = 0,\ f = 0,\ p_3 = 1 \qquad \eta = \infty: p_1 \to 0,\ p_3 \to 0 \quad \ldots(16)$$

Step 2: The finite difference method

The rectangular net is in the x and y planes, as shown in Fig. 2, and the following are the net points:

$$\xi^0 = 0,\ \xi^n = \xi^{n-1} + k_n,\ \ n = 1,2,3,\ldots,I \qquad \eta_0 = 0,\ \eta_j = \eta_{j-1} + h_j,\ j = 1,2,3,\ldots,J \quad \ldots(17)$$

Where k_n and h_j represent the $\Delta\xi$ and $\Delta\eta$ spacing, respectively.

$$\left(\frac{\partial(\ )}{\partial \xi}\right)^{n-1/2}_{j-1/2} = \frac{(\ )^n_{j-1/2} - (\ )^{n-1}_{j-1/2}}{k_n},\ \left(\frac{\partial(\ )}{\partial \eta}\right)^{n-1/2}_{j-1/2} = \frac{(\ )^{n-1}_{j-1/2} - (\ )^{n-1}_{j-1/2}}{k_n}$$

$$(\ )^{n-1/2}_j = \frac{(\ )^{n-1}_j + (\ )^n_j}{2},\ (\ )^n_{j-1/2} = \frac{(\ )^n_{j-1} + (\ )^n_j}{2} \quad \ldots(18)$$

The finite-difference form is computed using the central difference technique.

$$f' = p_1 \Rightarrow (p_1)^n_{j-1/2} = \frac{(p_1)^n_j + (p_1)^n_{j-1}}{2} = \frac{\left(f^n_j - f^n_{j-1}\right)}{h_j} \quad \ldots(19)$$

$$(p_1)' = p_2 \Rightarrow (p_2)^n_{j-1/2} = \frac{(p_2)^n_j + (p_2)^n_{j-1}}{2} = \frac{\left((p_1)^n_j - (p_1)^n_{j-1}\right)}{h_j} \quad \ldots(20)$$

$$(p_3)' = p_4 \Rightarrow (p_4)^n_{j-1/2} = \frac{(p_4)^n_j + (p_4)^n_{j-1}}{2} = \frac{\left((p_3)^n_j - (p_3)^n_{j-1}\right)}{h_j} \quad \ldots(21)$$

$$(p_4)' = p_5 \Rightarrow (p_5)^n_{j-1/2} = \frac{(p_5)^n_j + (p_5)^n_{j-1}}{2} = \frac{\left((p_4)^n_j - (p_4)^n_{j-1}\right)}{h_j} \quad \ldots(22)$$

The following Eqs. 19-22 are centred at the $\xi^{i-1/2}, \eta_{j-1/2}$ locations, which are shown below.

$$\left.\begin{array}{c}\left(1+\frac{1}{Ca}\right)\ \left(\frac{(p_2)^n_j - (p_2)^n_{j-1}}{h_j}\right)\ \left(\frac{\mu_{thnf}}{\mu_f}\right) + \\ (1+\alpha)\left(\frac{\rho_{thnf}}{\rho_f}\right)\ \left[\ \left(f^n_{j-1/2}(p_2)^n_{j-1/2}\right) - \left((p_1)^n_{j-1/2}\right)^2\right] + \\ \alpha\left[\left(\frac{\sigma_{thnf}}{\sigma_f}\right)\ M\ (p_1)^n_{j-1/2} + (p_2)^{n-1}_{j-1/2}\ (f)^n_{j-1/2} - f^{n-1}_{j-1/2}\ (p_2)^n_{j-1/2}\right] \\ + B(p_3)^n_{j-1/2}\end{array}\right\} =$$

$$-\left[\begin{array}{c}\left(\frac{(p_2)^n_j - (p_2)^{n-1}_{j-1}}{h_j}\right)\ \left(1+\frac{1}{\beta}\right)\ \left(\frac{\mu_{thnf}}{\mu_f}\right) + \\ \left(\frac{\rho_{thnf}}{\rho_f} - \alpha\right)\ \left(\left(f^{n-1}_{j-1/2}\right)\ (p_2)^{n-1}_{j-1/2}\right) + \\ A^*\ (p_1\ )^{n-1}_{j-1/2} + B^*\ (p_3)^{n-1}_{j-1/2} + \\ \left(\alpha - \frac{\sigma_{thnf}}{\sigma_f}\right)\ \left(p^{n-1}_{j-1/2}\right)^2\end{array}\right] \quad \ldots(23)$$

$$\frac{1}{\Pr}\left(\frac{(p_4)^n_j - (p_4)^{n-1}_{j-1}}{h_j}\right)\left(\frac{k_t}{k_f}\right) + (f^n_{j-1})\ (p_4)^n_{j-1}\ (1+\alpha) - ((p_1)^n_{j-1}\ (p_3)^n_{j-1}) + A^*\ (p_1)^n_{j-1} + B^*\ (p_3)^n_{j-1} + \alpha\ (p_3)^{n-1}_{j-1/2}\ (p_1)^n_{j-1/2} - \alpha(p_1)^{n-1}_{j-1/2}\ (p_3)^n_{j-1/2} - \alpha\left(f^{n-1}_{j-1/2}\right)(p_4)^n_{j-1/2} + \alpha\ (p_4)^{n-1}_{j-1/2}\left(f^n_{j-1/2}\right)$$

$$= -\left[\begin{array}{c}\frac{1}{\Pr}\left(\frac{(p_4)^n_j - (p_4)^{n-1}_{j-1}}{h_j}\right)\left(\frac{k_t}{k_f}\right) + (1-\alpha)\ (f\,p_4)^{n-1}_{j-1/2} + \\ A^*(p_1)^{n-1}_{j-1} + B^*\ (p_4)^{n-1}_{j-1/2} + \alpha\ (\ (p_1)\ (p_3)\ )^{n-1}_{j-1/2}\end{array}\right] \quad \ldots(24)$$

Where $\alpha = \frac{\xi^{n-1/2}}{k_n}$, $B = \frac{\sin\left(\xi^{n-1/2}\right)}{\xi^{n-1/2}}$

The boundary conditions are

$$f^i_0 = (p_1)^i_0 = 0,\ (p_3)^i_0 = 1 \qquad (p_1)^i_J \to 1,\ \ (p_3)^i_J \to 0 \quad \ldots(25)$$

Step 3:Newton's linearization approach

Using well-known techniques $(f)^{n-1}_j, (p_1)^{n-1}_j, (p_2)^{n-1}_j, (p_3)^{n-1}_j, (p_4)^{n-1}_j, (p_5)^{n-1}_j$ the unknown $(f)^n_j, (p_1)^n_j, (p_2)^n_j, (p_3)^n_j, (p_4)^n_j, (p_5)^n_j$ are predicted to be $0 \le j \le J$.

$$\left(f^n_j, (p_1)^n_j, (p_2)^n_j,\ (p_3)^n_j, (p_4)^n_j\right) \equiv \left(f_j, (p_1)_j, (p_2)_j, (p_3)_j, (p_4)_j\right).$$

The collection of equations of central difference is denoted as

$$\frac{(p_1)_j + (p_1)_{j-1}}{2} = \frac{f_j - f_{j-1}}{h_j} \quad \ldots(26)$$

$$\frac{(p_2)_j + (p_2)_{j-1}}{2} = \frac{(p_1)_j - (p_1)_{j-1}}{h_j} \quad \ldots(27)$$

$$\frac{(p_4)_j + (p_4)_{j-1}}{2} = \frac{(p_3)_j - (p_3)_{j-1}}{h_j} \quad \ldots(28)$$

$$\frac{(p_6)_j + (p_6)_{j-1}}{2} = \frac{(p_5)_j - (p_5)_{j-1}}{h_j} \quad \dots (29)$$

$$\left(1+\frac{1}{Ca}\right)\left((p_2)_j-(p_2)_{j-1}\right)\left(\frac{\mu_{thnf}}{\mu_f}\right) + h_j\left(\frac{\rho_{thnf}}{\rho_f}\right)\left(\frac{(1+\alpha)h_j}{4}(f_j+f_{j-1})\left((p_2)_j+(p_2)_{j-1}\right)\right) - h_j\left(\frac{\rho_{thnf}}{\rho_f}\right)\left((p_1)_j+(p_1)_{j-1}\right)^2\left(\frac{1+\alpha}{4}\right) + h_j\left(\frac{\sigma_{thnf}}{\sigma_f}\right)\frac{\alpha M}{2}\left((p_1)_j+(p_1)_{j-1}\right) + \frac{\alpha h_j}{2}(p_2)^{n-1}_{j-1/2}\left(f_j+f_{j-1}\right) - \alpha f^{n-1}_{j-1/2}\left((p_1)_j+(p_1)_{j-1}\right) + \frac{Bh_j}{2}\left((p_3)_j+(p_3)_{j-1}\right) = [\Pi_1]^{n-1}_{j-1/2} \quad \dots(30)$$

$$\frac{1}{\Pr}\left((p_4)_j-(p_4)_{j-1}\right)\left(\frac{k_t}{k_f}\right) + h_j\left(\frac{1+\alpha}{4}\right)(f_j+f_{j-1})\left((p_4)_j+(p_4)_{j-1}\right) - \frac{\alpha h_j}{4}\left((p_1)_j+(p_1)_{j-1}\right)\left((p_3)_j+(p_3)_{j-1}\right) + \frac{A^* h_j}{2}\left((p_1)_j+(p_1)_{j-1}\right) + \frac{B^* h_j}{2}\left((p_3)_j+(p_3)_{j-1}\right) + \frac{\alpha h_j}{2}(p_3)^{n-1}_{j-1/2}\left((p_1)_j+(p_1)_{j-1}\right) - \frac{\alpha h_j}{2}(p_1)^{n-1}_{j-1/2}\left((p_3)_j+(p_3)_{j-1}\right) - \frac{\alpha h_j}{2}\left(f^{n-1}_{j-1/2}\right)\left((p_4)_j+(p_4)_{j-1}\right) + \frac{\alpha h_j}{2}\left((p_4)^{n-1}_{j-1/2}\right)(f_j+f_{j-1}) = [\Pi_2]^{n-1}_{j-1/2} \quad \dots(31)$$

$$[\Pi_1]^{n-1}_{j-1/2} = -h_j\left[\begin{array}{c}\left(\frac{(p_2)^n_j-(p_2)^n_{j-1}}{h_j}\right)\left(1+\frac{1}{Ca}\right)\left(\frac{\mu_{thnf}}{\mu_f}\right)+\left(\frac{\rho_{thnf}}{\rho_f}-\alpha\right)\left(\left(f^{n-1}_{j-1/2}\right)(p_2)^{n-1}_{j-1/2}\right)+ \\ A^*\left(p_1\right)^{n-1}_{j-1/2} + B^*(p_3)^{n-1}_{j-1/2} + \left(\alpha-\frac{\sigma_{thnf}}{\sigma_f}\right)\left(p^{n-1}_{j-1/2}\right)^2\end{array}\right] \quad \dots(32)$$

$$[\Pi_2]^{n-1}_{j-1/2} = -h_j\left[\begin{array}{c}\frac{1}{\Pr}\left(\frac{(p_4)^n_j-(p_4)^n_{j-1}}{h_j}\right)\left(\frac{k_t}{k_f}\right) + (1-\alpha)\left(f\,p_4\right)^{n-1}_{j-1/2} + A^*(p_1)^{n-1}_{j-1} + \\ B^*(p_4)^{n-1}_{j-1/2} + \alpha\left((p_1)(p_3)\right)^{n-1}_{j-1/2}\end{array}\right] \quad \dots(33)$$

Where $[\prod_1 \ ]^{n-1}_{j-1/2}, [\prod_2 \ ]^{n-1}_{j-1/2}$ are the known quantities.

Below presented Newton's method to convert to a nonlinear collection of equations approach.

$$\Delta f_j^{(n)} + f_j^n = f_j^{(n+1)} \quad \dots(34)$$

$$\Delta(p_1)_j^{(n)} + (p_1)_j^{(n)} = (p_1)_j^{(n+1)} \quad \dots(35)$$

$$\Delta(p_2)_j^{(n)} + (p_2)_j^{(n)} = (p_2)_j^{(n+1)}. \quad \dots(36)$$

$$\Delta(p_3)_j^{(n)} + (p_3)_j^{(n)} = (p_3)_j^{(n+1)} \quad \dots(37)$$

$$\Delta(p_4)_j^{(n)} + (p_4)_j^{(n)} = (p_4)_j^{(n+1)} \quad \dots(38)$$

The statement is enforced in Eqs. 26-38 with the higher-order of (Δ) removed.

$$\Delta f_j - \Delta f_{j-1} - \frac{h_j}{2}\Delta(p_1)_j - \frac{h_j}{2}\Delta(p_1)_{j-1} - (l_1)_j = 0 \quad \dots(39)$$

$$\Delta(p_1)_j - \Delta(p_1)_{j-1} - \frac{h_j}{2}\Delta(p_2)_j - \frac{h_j}{2}\Delta(p_2)_{j-1} - (l_2)_j = 0 \quad \dots(40)$$

$$\Delta(p_3)_j - \Delta(p_3)_{j-1} - \frac{h_j}{2}\Delta(p_4)_j - \frac{h_j}{2}\Delta(p_4)_{j-1} - (l_3)_j = 0 \quad \dots(41)$$

$$\begin{array}{c}(G_1)_j\Delta(p_2)_j + (G_2)_j\Delta(p_2)_{j-1} + (G_3)_j\Delta f_j \\ +(G_4)_j\Delta f_{j-1} + (G_5)_j\Delta(p_1)_j + \\ (G_6)_j\Delta(p_1)_{j-1} + (G_7)_j\Delta(p_3)_j \\ +(G_8)_j\Delta(p_3)_{j-1} - (l_4)_j = 0\end{array} \quad \dots(42)$$

$$\begin{array}{c}(H_1)_j\Delta(p_4)_j + (H_2)_j\Delta(p_4)_{j-1} \\ +(H_3)_j\Delta(f_j) + (H_4)_j\Delta(f_{j-1}) \\ +(H_5)_j\Delta(p_1)_j + (H_6)_j\Delta(p_1)_{j-1} \\ +(H_7)_j\Delta(p_3)_j + (H_8)_j\Delta(p_3)_{j-1} - (l_5)_j = 0\end{array} \quad \dots(43)$$

Where:

$$(G_1)_j = \left(\frac{\mu_{thnf}}{\mu_f}\right)\left(1+\frac{1}{Ca}\right) + \left(\frac{\rho_{thnf}}{\rho_f}\right)\left(\frac{(1+\alpha)\,h_j}{2}\right)\left(f_{j-1/2}\right)$$

$$(G_2)_j = -\left(\frac{\mu_{thnf}}{\mu_f}\right)\left(1+\frac{1}{Ca}\right) + \left(\frac{\rho_{thnf}}{\rho_f}\right)\left(\frac{(1+\alpha)\,h_j}{2}\right)\left(f_{j-1/2}\right)$$

$$(G_3)_j = \left(\frac{\rho_{thnf}}{\rho_f}\right)\left(\frac{(1+\alpha)\,h_j}{2}\right)(p_2)_{j-1/2} - \frac{\alpha}{2}h_j f^{n-1}_{j-1/2}$$

$$(G_4)_j = \left(\frac{\rho_{thnf}}{\rho_f}\right)\left(\frac{(1+\alpha)\,h_j}{2}\right)(p_2)_{j-1/2} - f^{n-1}_{j-1/2}\frac{\alpha}{2}h_j$$

$$(G_5)_j = -\left(\frac{h_j(1+\alpha)}{2}\right)\left(\frac{\rho_{thnf}}{\rho_f}\right)(p_1)_{j-1/2} + \left(\frac{\alpha h_j}{2}\right)\left(\frac{\sigma_{thnf}}{\sigma_f}\right)M$$

$$(G_6)_j = -\left(\frac{h_j(1+\alpha)}{2}\right)\left(\frac{\rho_{thnf}}{\rho_f}\right)(p_1)_{j-1/2} + \left(\frac{\alpha h_j}{2}\right)\left(\frac{\sigma_{thnf}}{\sigma_f}\right)M$$

$$(G_7)_j = -\frac{Bh_j}{2}$$

$$(G_8)_j = -\frac{Bh_j}{2}$$

$$(H_1)_j = \frac{1}{\Pr}\left(\frac{k_t}{k_f}\right) + f_{j-1/2}\left(\frac{(1+\alpha)}{h_j}\right) - f_{j-1/2}^{n-1}\frac{\alpha h_j}{2}$$

$$(H_2)_j = -\frac{1}{\Pr}\left(\frac{k_t}{k_f}\right) + f_{j-1/2}\left(\frac{(1+\alpha)}{h_j}\right) - f_{j-1/2}^{n-1}\frac{\alpha h_j}{2}$$

$$(H_3)_j = (p_4)_{j-1/4}\left(\frac{(1+\alpha)h_j}{2}\right) + \frac{\alpha h_j}{2}p_{j-1/2}^{n-1}$$

$$(H_4)_j = (p_4)_{j-1/4}\left(\frac{(1+\alpha)h_j}{2}\right) + \frac{\alpha h_j}{2}p_{j-1/2}^{n-1}$$

$$(H_5)_j = -\frac{\alpha h_j}{2}(p_3)_{j-1/2} + \frac{A^* h_j}{2} + \frac{\alpha h_j}{2}(p_3)_{j-1/2}^{n-1}$$

$$(H_6)_j = -\frac{\alpha h_j}{2}(p_3)_{j-1/2} + \frac{A^* h_j}{2} + \frac{\alpha h_j}{2}(p_3)_{j-1/2}^{n-1}$$

$$(H_7)_j = -\frac{\alpha h_j}{2}(p_1)_{j-1/2} + \frac{B^* h_j}{2} - \frac{\alpha h_j}{2}(p_1)_{j-1/2}^{n-1}$$

$$(H_8)_j = -\frac{\alpha h_j}{2}(p_1)_{j-1/2} + \frac{B^* h_j}{2} - \frac{\alpha h_j}{2}(p_1)_{j-1/2}^{n-1}$$

$$(r_4)_{j-1/2} = ((p_2)_{j-1} - (p_2)_j)\left(1+\frac{1}{Ca}\right)\left(\frac{\mu_{thnf}}{\mu_f}\right) - h_j\left(\frac{\rho_{thnf}}{\rho_f}\right)(1+\alpha)\left(f(p_2)\right)_{j-1/2} + (1+\alpha)\left((p_1)_{j-1/2}\right)^2\left(\frac{\rho_{thnf}}{\rho_f}\right)h_j - \alpha\left(\frac{\sigma_{thnf}}{\sigma_f}\right)M(p_1)_{j-1/2}h_j - B^* h_j(p_3)_{j-1/2} - \alpha h_j(p_2)_{j-1/2}^{n-1}\left(f_{j-1/2}\right) + \alpha h_j f_{j-1/2}^{n-1}(p_2)_{j-1/2} + [\Pi_1]_{j-1/2}^{n-1} \quad \ldots(44)$$

$$(r_5)_{j-1/2} = \frac{1}{\Pr}((p_4)_{j-1} - (p_4)_j)\left(\frac{k_t}{k_f}\right) - (1+\alpha)\left(\left(f_{j-1/2}\right)(p_4)_{j-1/2}\right)h_j + \alpha h_j\left((p_1)_{j-1/2}(p_3)_{j-1/2}\right) + A^* h_j(p_1)_{j-1/2} - B^* h_j(p_3)_{j-1/2} - \alpha h_j(p_3)_{j-1/2}^{n-1}(p_1)_{j-1/2} + \alpha h_j(p_1)_{j-1/2}^{n-1}(p_3)_{j-1/2} + \alpha h_j f_{j-1/2}^{n-1}\left((p_4)_{j-1/2}\right) - \alpha h_j(p_4)_{j-1/2}^{n-1}\left(f_{j-1/2}\right) + [\Pi_2]_{j-1/2}^{n-1} \quad \ldots(45)$$

With the boundary conditions

$$\Delta f_0^n = 0,\ \Delta(p_1)_0^n = 0,\ \Delta(p_3)_0^n = 0,\ \Delta(p_1)_J^n = 0,\ \Delta(p_3)_J^n = 0,\ f_0^n = (p_1)_0^n = 0,\ ((p_3)_0^1) = 1,\ (p_1)_J^n = 0,\ (p_3)_J^n = 0 \quad \ldots(46)$$

Step 4: Tridiagonal System of Solution

The block-elimination approach may be used to solve the linearized difference Eqn. (39)-(46) by Cebeci and Bradshaw o on[34]. because the system is block-tridiagonal in structure. The block-tridiagonal structure is often made up of variables or constants, but in this case, an unusual aspect is that it is made up of block matrices, Eqn. (39)-(46) may be represented in matrix-vector form as

$$Q\ \Omega = l \quad \ldots(47)$$

Where;

$$Q = \begin{bmatrix} [Q_1]\,[S_1] & & & \\ [R_2]\,[Q_2]\,[S_2] & \ddots & & \\ & \ddots & \ddots & \\ & & [R_{j-1}]\,[Q_{j-1}]\,[S_{j-1}] & \\ & & [R_j]\,[Q_j] & \end{bmatrix}$$

$$\Omega = \begin{bmatrix} [\Omega_1] \\ [\Omega_2] \\ \vdots \\ [\Omega_{j-1}] \\ [\Omega_j] \end{bmatrix} \quad and \quad l = \begin{bmatrix} [l_1] \\ [l_2] \\ \vdots \\ [l_{j-1}] \\ [l_j] \end{bmatrix}$$

The matrix components the following

$$-\frac{h_j}{2} = -z$$

$$[Q_1] = \begin{bmatrix} 0 & 0 & 1 & 0 & 0 \\ -z & 0 & 0 & -z & 0 \\ 0 & -z & 0 & 0 & -z \\ (G_2) & 0 & (G_3) & (G_1) & 0 \\ 0 & (H_2) & (H_3) & 0 & (H_1) \end{bmatrix}$$

For $J \geq j \geq 2$:

$$[Q_J] = \begin{bmatrix} -Z & 0 & 1 & 0 & 0 \\ -1 & 0 & 0 & -Z & 0 \\ 0 & -1 & 0 & 0 & -Z \\ (G_6) & (G_8) & (G_3) & (G_1) & 0 \\ (H_6) & (H_8) & (H_3) & 0 & (H_1) \end{bmatrix}, J \geq j \geq 2$$

$$|R_J| = \begin{bmatrix} 0 & 0 & -1 & 0 & 0 \\ 0 & 0 & 0 & -z & 0 \\ 0 & 0 & 0 & 0 & -z \\ 0 & 0 & (G_4) & (G_2) & 0 \\ 0 & 0 & (H_4) & 0 & (H_1) \end{bmatrix}, 2 \leq j \geq J$$

$J - 1 \geq j \geq 1$:

$$|S_J| = \begin{bmatrix} -z & 0 & 0 & 0 & 0 \\ 1 & 0 & 0 & 0 & 0 \\ 0 & 1 & 0 & 0 & 0 \\ (G_5) & (G_7) & 0 & 0 & 0 \\ (H_5) & (H_7) & 0 & 0 & 0 \end{bmatrix}, 2 \leq j \geq J$$

$J \geq j \geq 2$:

$$[\Omega_1] = \begin{bmatrix} \Omega(p_1)_0 \\ \Omega(p_3)_0 \\ \Omega(f)_1 \\ \Omega(p_1)_1 \\ \Omega(p_2)_1 \end{bmatrix}, \quad [\Omega_j] = \begin{bmatrix} \Omega(p_1)_{J-1} \\ \Omega(p_3)_{J-1} \\ \Omega(f)_J \\ \Omega(p_1)_J \\ \Omega(p_2)_J \end{bmatrix}$$

$J \geq j \geq 1$:

$$[l_j] = \begin{bmatrix} (l_1)_{j-1/2} \\ (l_2)_{j-1/2} \\ (l_3)_{j-1/2} \\ (l_4)_{j-1/2} \\ (l_5)_{j-1/2} \end{bmatrix}$$

The linearized solution system is transformed utilising the Thomas technique, into a block tridiagonal form (Cebeci and Bradshaw[34]). Regarding the calculation, the spatial nodes (ξ, η) are set to 0.05. To increase the correctness of the result, the convergence criteria as set (10^{-6}) in this present computation.

4 Results and Discussion

The leading boundary layer equations are solved using Thomas algorithm and numerical computations are carried with MATLAB software to show the impact of various pertinent physical parameters on the flow field and engineering quantities through Figs. 3-42. Here maximum value of (η, ξ) is taken for which the boundary conditions are satisfied. Throughout the calculations, the parametric values are fixed as $\xi = 1.0, \Pr = 0.7, A = B = 0.1$ $M = 1.0, S_F = S_T = 0.5, Ca = 1.0$. Taken $A^* = A, B^* = B$ All the graphs therefore correspond to these values with variation the active variable $(M = 0.0,0.2,0.4,0.6)$ non-Newtonian Casson parameter $(\beta = 0.5,1.0,1.5,2.0)$ non- uniform energy production parameter $(A = B = 0.0,0.1,0.2,0.3)$, velocity slip $(S_F = 0.0,0.5,1.0,1.5)$, thermal slip parameter $(S_T = 0.5,1.0,1.5,2.0)$ and suction parameter $(S = 0.0,0.5,1.0,1.5)$. Figures (3-23) represent and describe the physical behaviour of these findings. The fluid properties of different nanoparticles are tabulated in Table 1. The current numerical method is compared with existing literature of and found a good agreement. The new findings are compared with prior impressive research of Yih[29]& Prasad *et al.*[33] that demonstrated great agreement to corroborate Keller box approachas shown in Table 2. This problem uses trihybrid nanofluid (TiO_2, Al_2O_3, SiO_2) with water as poor conducting fluid. The nanofluid, hybrid nanofluid and tri-hybrid nanoflow combinations are $(H_2O+TiO_2, H_2O+TiO_2+Al_2O_3, H_2O+TiO_2+Al_2O_3+SiO_2)$ Figs. 3 & 4 show how magnetic force field forces the velocity and temperature of nanofluids, hybrid nanofluids, and ternary hybrid nanofluids. The presence of external body force called magnetic field produces a contracting force known as the Lorentz force, which opposes fluid movement. As a result, increasing M intensifies the Lorentz force. This decreases the flow velocity enables nanoparticles to transmit more heat, resulting in an increase in the flow temperature. The fluid energy of tri-hybrid nanofluid $(H_2O, TiO_2, Al_2O_3, SiO_2)$ is superior to those of fluid, nanofluid (H_2O, TiO_2) and hybrid nanofluid (H_2O, TiO_2, Al_2O_3).

Figures 5 & 6 show the effect of Casson fluid property on both temperature and velocity curves. As the $(Ca = 0.5,1.0,1.5,2.0)$ value increases, the value of the velocity graphic decreases. For larger Ca, the fluid behaves like Newtonian getting deviated from elasticity. The slight uplift in nanoflow temperature is

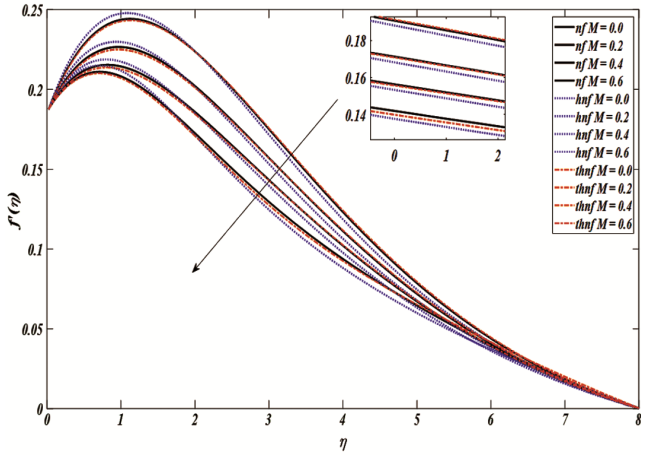

Fig. 3 — The effect of (M) on $f'(\eta)$.

Table 1 — Thermophysical properties of the nanoparticles and the base fluid[35].

	$\left[kgm^{-1}\right]\rho$	$\left[Sm^{-1}\right]\sigma$	$\left[W(mk)^{-1}\right]k$
H_2O	997.1	5.5×10^{-6}	0.6071
TiO_2	4250	2.4×10^{6}	8.953
SiO_2	2270	3.5×10^{6}	1.4013
Al_2O_3	6310	5.965×10^{7}	32.9

Table 2 — Local heat transfer coefficient (Nu) values for varied (ξ) values $Ca = 0, S = 0, N_0 = 0, K_0 = 0$.

(ξ)	Yih[29] $-\theta'(\xi,0)$	Ramachandra *et al.*[33] $-\theta'(\xi,0)$	Present Study $-\theta'(\xi,0)$
0.0	0.4214	0.4213	0.4211
0.2	0.4207	0.4206	0.4204
0.4	0.4184	0.4185	0.4182
0.6	0.4147	0.4146	0.4153
0.8	0.4096	0.4095	0.4092
1.0	0.4030	0.4031	0.4028
1.2	0.3950	0.3947	0.3945
1.4	0.3854	0.3857	0.3854
1.6	0.3740	0.3733	0.3730
1.8	0.3608	0.3602	0.3598
2.0	0.3457	0.3458	0.3457
2.2	0.3283	0.3280	0.3268
2.4	0.3086	0.3079	0.3076
2.6	0.2860	0.2858	0.2856
2.8	0.2595	0.2590	0.2588
3.0	0.2267	0.2261	0.2258
π	0.1962	0.1961	0.1959

seen Fig. 6, which is same as the case of Ramachandra *et al.*[33]. Hybrid nanoflow has more impact on the fluid movement than the nanoflow which is superior to hybrid flow case.

Figures 7 & 8 show significant effect of heat and velocity as the thermal slip parameter (S_T = 0.5,1.0,1.5,2.0) enhances. The velocity response near the surface of cylinder is in uplift, after η~2 the profiles fall. The highest velocity is associated with the least value of thermal slip ($S_T = 0.5$) The greatest deceleration occurs in the event of the greatest thermal slip value ($S_T = 2.0$). Temperature (Fig. 8) drops as thermal slip upsurges the greatest impact is seen near the wall. All measurements of temperature converge neatly to zero later into the unrestricted stream. As η rises, the velocity slows down and decays to zero.

The effect of the velocity slip on momentum and energy of nanoflow distributions is seen in Figs 9 & 10. When the slip parameter (S_F = 0.0,0.5,1.0,1.5) is increased, the momentum component with no dimensions near the boundary is much decreased. The effect of S_F is clearly higher near the cylinder surface ($\eta = 0$). Smooth decay of the velocity profiles into the free stream are seen, demonstrating good numerical convergence. The energy profiles decays as its boundary layer will decrease correspondingly. Fig. 10 shows that the temperature $\theta(\eta)$ declines sharply as the radial coordinate increases.

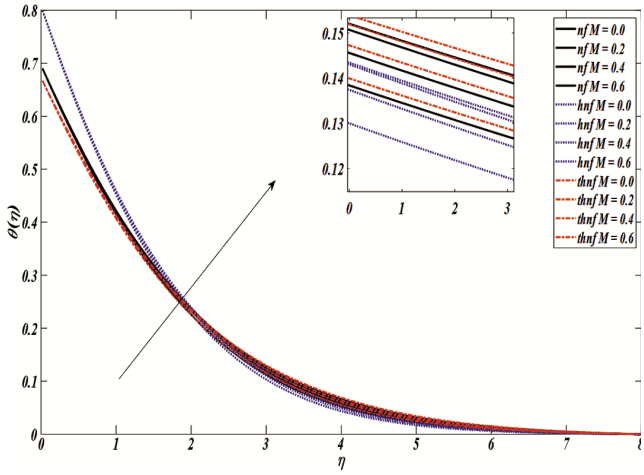

Fig. 4 — The effect of (M) on $\theta(\eta)$.

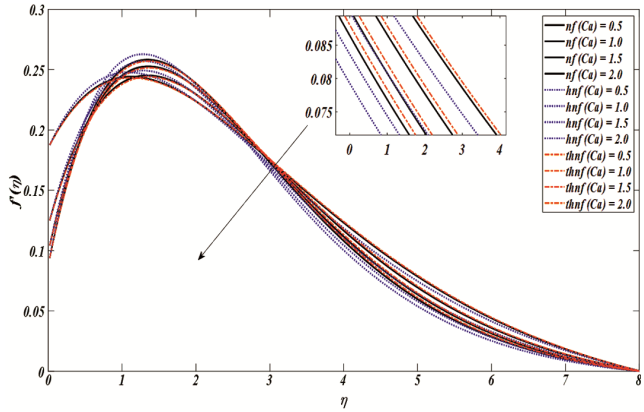

Fig. 5 — The effect of (Ca) on $f'(\eta)$.

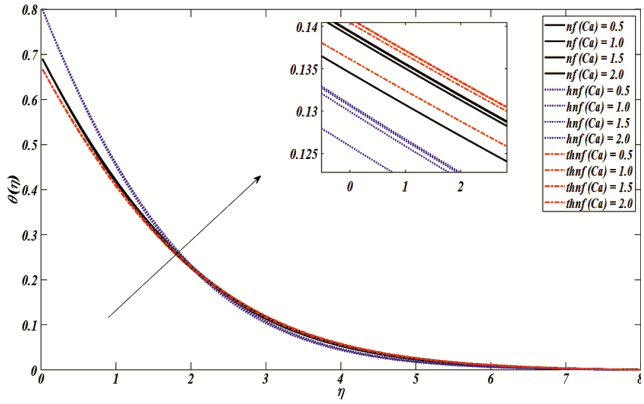

Fig. 6 — The effect of (Ca) on $\theta(\eta)$.

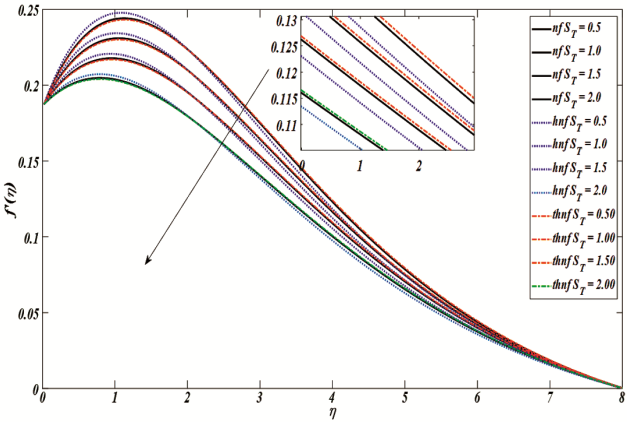

Fig. 7 — The effect of (S_T) on $f'(\eta)$.

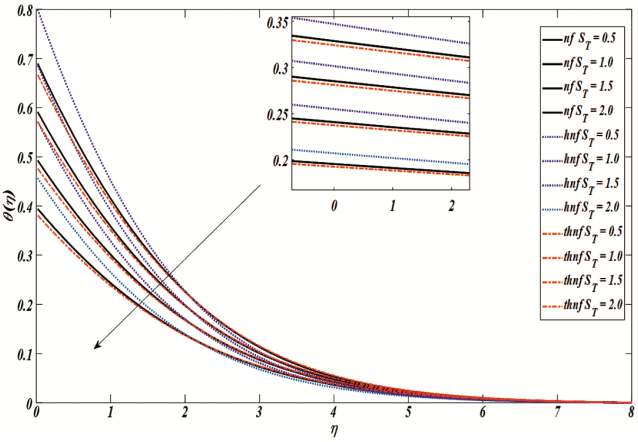

Fig. 8 — The effect of (S_T) on $\theta(\eta)$.

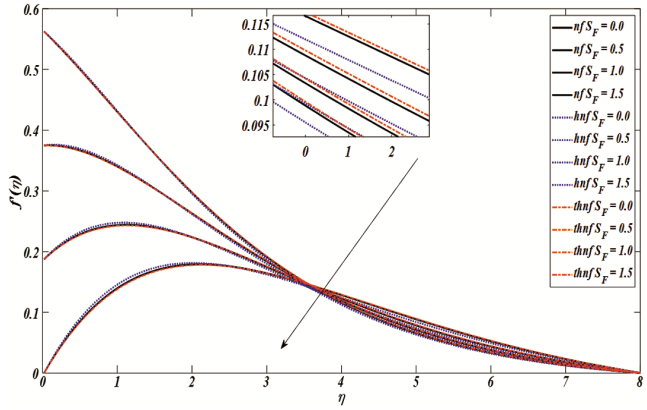

Fig. 9 — The effect of (S_F) on $f'(\eta)$.

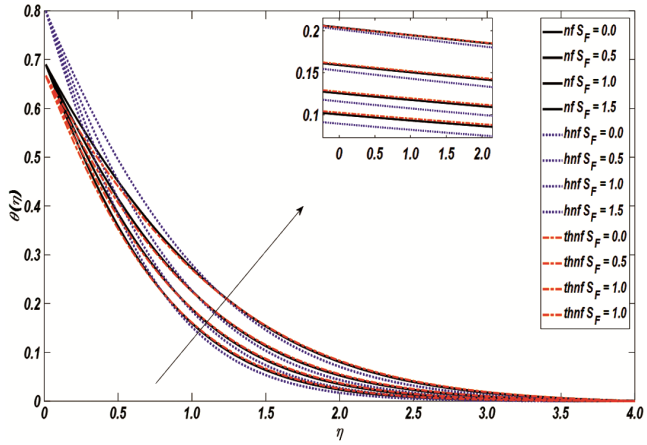

Fig. 10 — The effect of (S_F) on $\theta(\eta)$.

Figures 11 & 12 show how drag suction impacts the flow acceleration and heat curves as a function of the radial distance (η). When the drag increases $(S > 0,0.5,1.0,1.5)$ the velocity obviously decreases, indicating that the flow velocity boundary layer has shortened its thickness. *i.e.*, as suction increases, the outermost boundary layer clings closer to the fluid flow. Raising suction is an ideal cool control method for cylinder's exterior flow. Temperature (θ) decreasing significantly with increasing blowing at the cylinder surface and falls with improved suction.

Figures. 13 & 14 show that the irregular source of heat generation effect (A) on the fluid momentum and energy profiles. Increases in A, $(A = 0.0,0.1,0.2,0.3)$ both momentum and energy profiles increase. Figs 15 & 16 show that irregular source of heat variable impact on velocity and temperature. Increases the $(B = 0.0,0.1,0.2,0.3)$ values the velocity profiles increase, and temperature profiles increase. The existence of a heat source $(A, B > 0)$ contributes extra energy to the thermal boundary layer, raising the fluid temperatures, while a heat sink

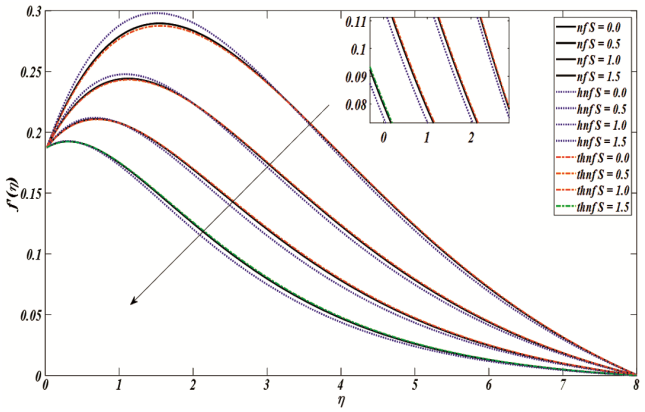

Fig. 11 — The effect of (S) on $f'(\eta)$.

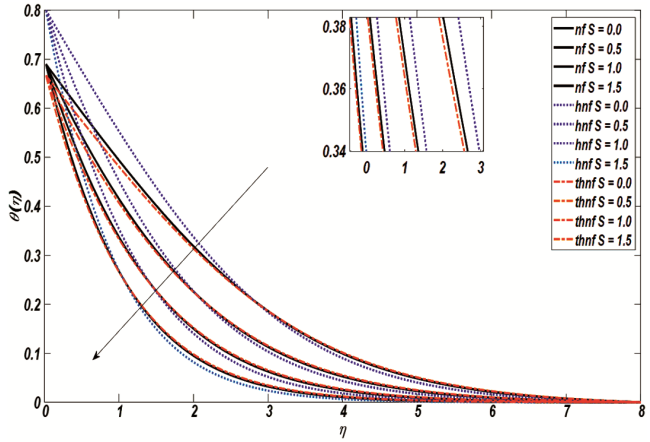

Fig. 12 —The effect of (S) on $\theta(\eta)$.

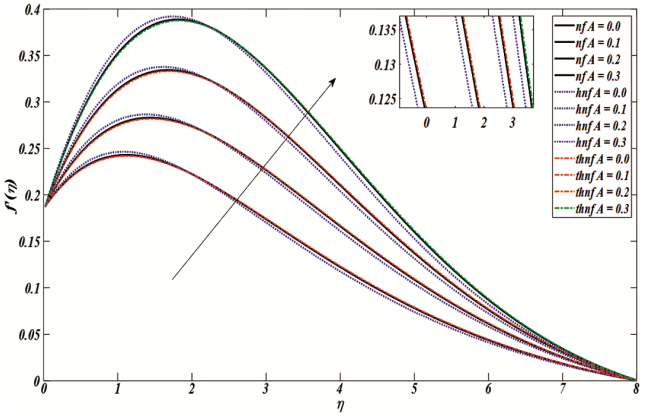

Fig. 13 — The effect of (A) on $f'(\eta)$.s

$(A, B < 0)$ absorbed a boundary layer thermal energy, lowering the temperature of the fluid.

Figures 17–30 show the distribution of streamlines (ψ) The reaction of the streamlines (ψ) with (M) and (Ca) is shown. In Figs. 17-39, declined fluid speed is observed in the absence of (Ca) and (ψ) (no convective heat transfer), but flow patterns are

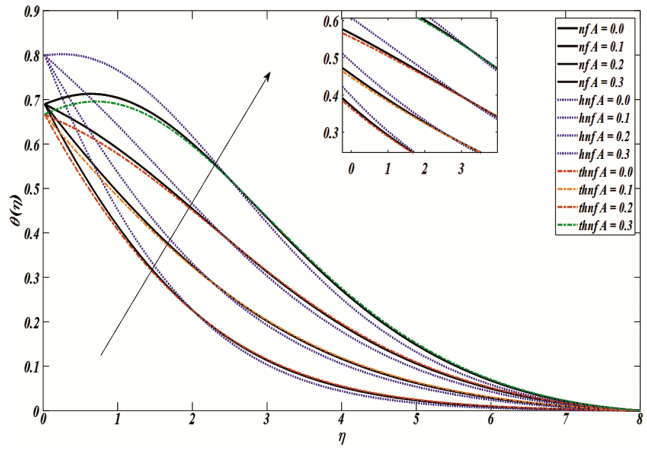

Fig 14 — The effect of (A) on $\theta(\eta)$.

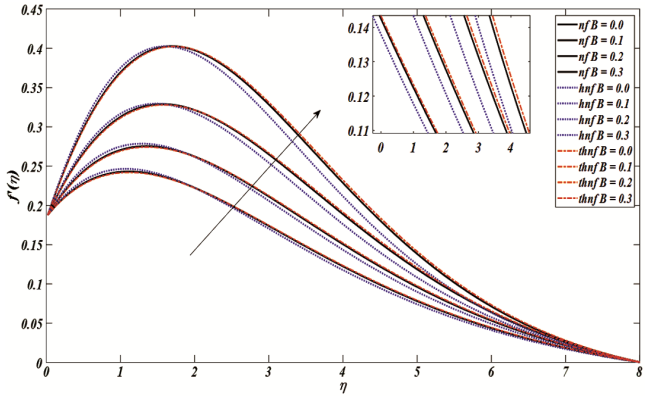

Fig. 15 — The effect of (B) on $f'(\eta)$.

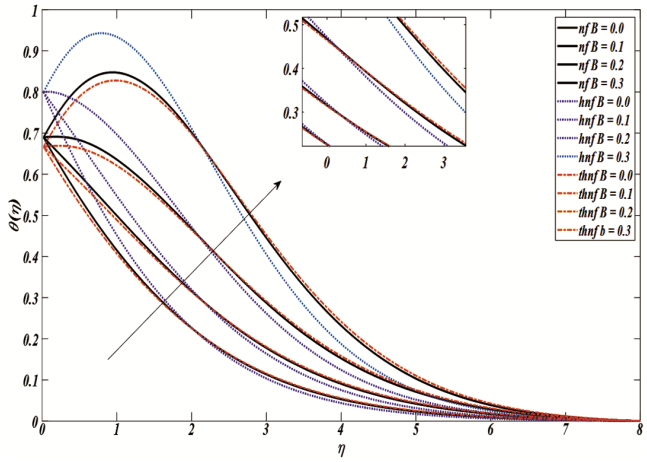

Fig. 16 — The effect of (B) on $\theta(\eta)$.

raised with increasing levels. The M (0.0, 0.3, 0.6, 0.9) values of the nano fluid, tri nanofluid mixture and hybrids nanofluid graphs are shown in Figs. 17-28, and the $(\beta = 0.0,0.3,0.6,0.9)$ values of the nano fluid, tri nanofluid mixture and hybrids nanofluid graphs are shown in Figs. 29-30.

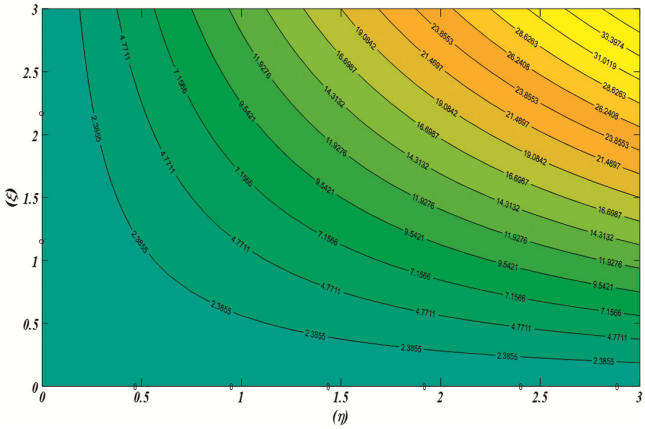

Fig. 17 — Streamlines for increasing $(M = 0)$ values in nanofluids.

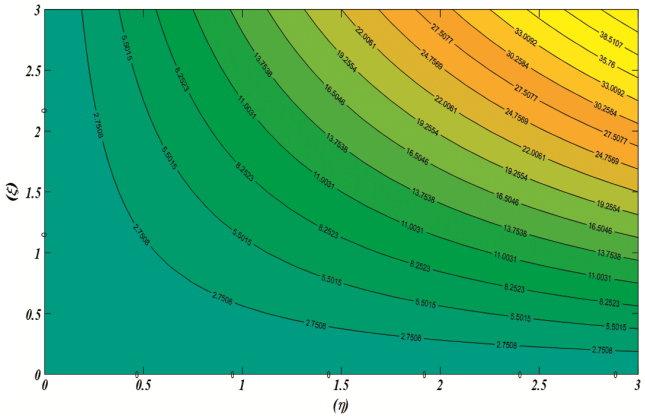

Fig. 18 — Streamlines for increasing $(M = 0.3)$ values in nanofluids.

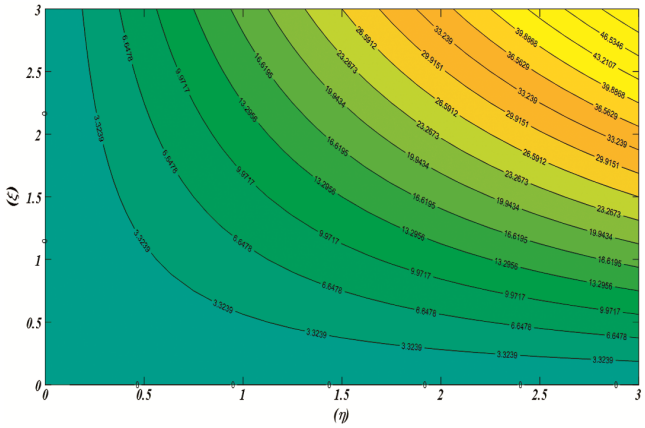

Fig. 19 — Streamlines for increasing $(M = 0.6)$ values in nanofluids.

Figures. 31 & 31 demonstrate the influence of parameter (M, S_T) modification on skin friction coefficient (Cf) and the local Nusselt number (Nu). Increase in M values establishes a relationship between the coefficient of friction with the surface. It is seen that magnetic force reduces the friction force

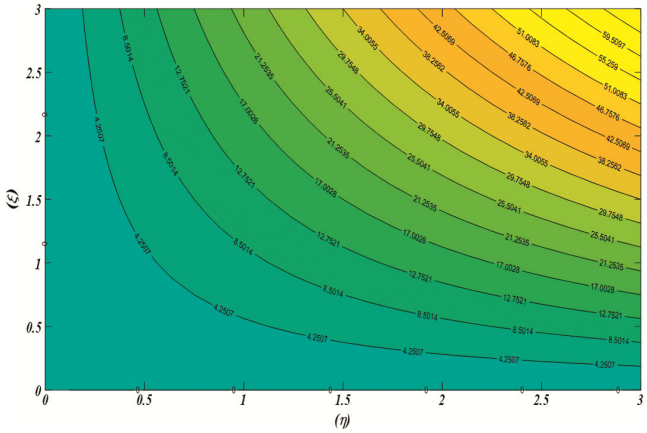

Fig. 20 — Streamlines for increasing ($M = 0.9$) values in nanofluids.

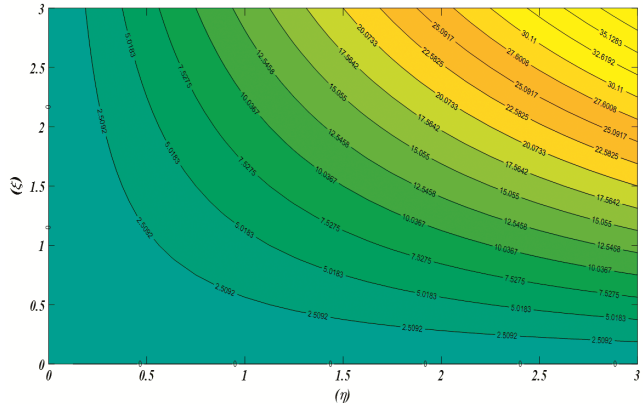

Fig. 21 — Streamlines for increasing ($M = 0.0$) values in hybridity nanofluid.

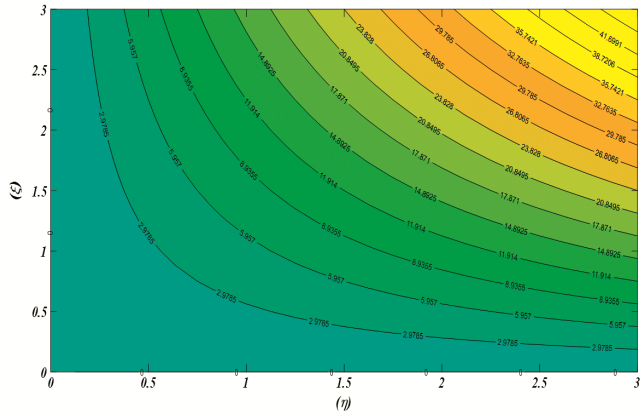

Fig. 22 — Streamlines for increasing ($M = 0.3$) values in hybridity nanofluid.

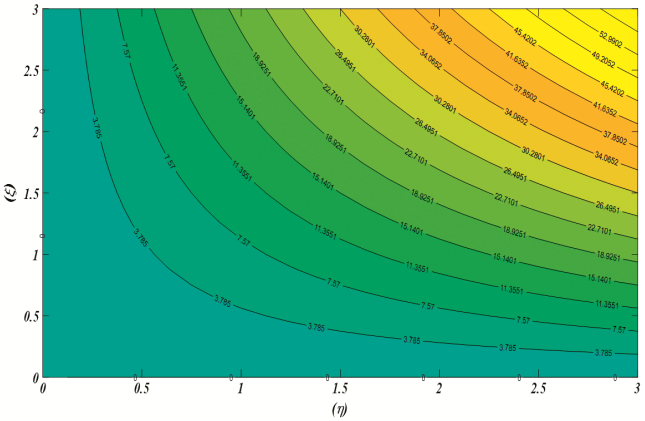

Fig. 23 — Streamlines for increasing ($M = 0.6$) values in hybridity nanofluid.

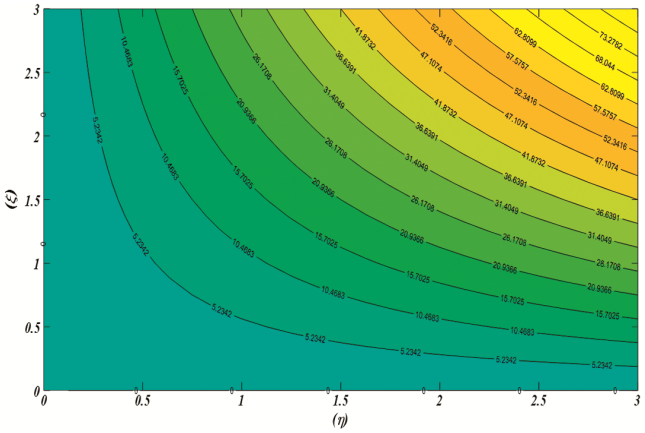

Fig. 24 — Streamlines for increasing ($M = 0.9$) values in hybrid nanofluids.

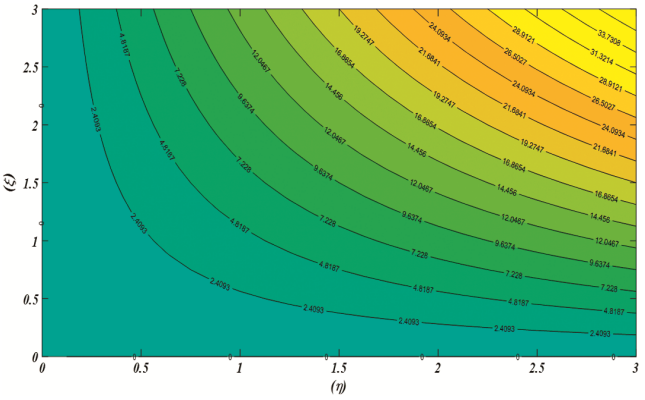

Fig. 25 — Streamlines for increasing ($M = 0.0$)values in ternary hybridity nanofluid.

at the surface and reduces the heat transfer rate. it has been discovered that increasing thermal slip S_T reduces both the Nusselt number and skin friction coefficient (*Cf*) (Figs 33 & 34).

Figures 35 & 36 show the influence of the Casson parameter (*Ca*) on the skin friction (*Cf*) and the local Nusselt number (*Nu*). The skin friction coefficient rises as (*Ca)* grows because, as previously calculated, greater values of (*Ca*) increase flow$f'(\eta)$. Larger (Ca) values correlate to a gradual reduction in Casson fluid yield stress *i.e.*, a diminution in rheological properties. Higher (*Ca*) values bring the flow closer to

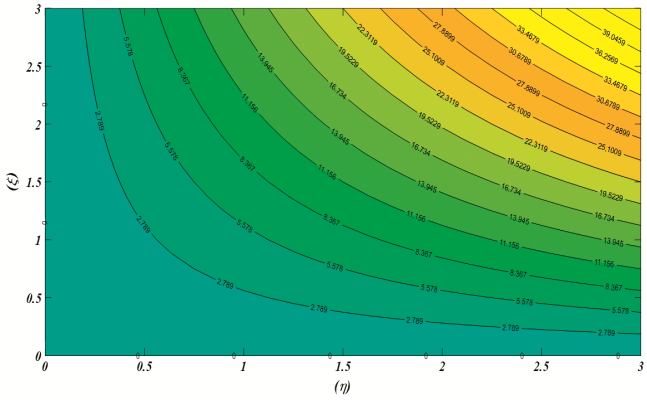

Fig. 26 — Streamlines for increasing ($M = 0.3$) values in ternary hybridity nanofluid.

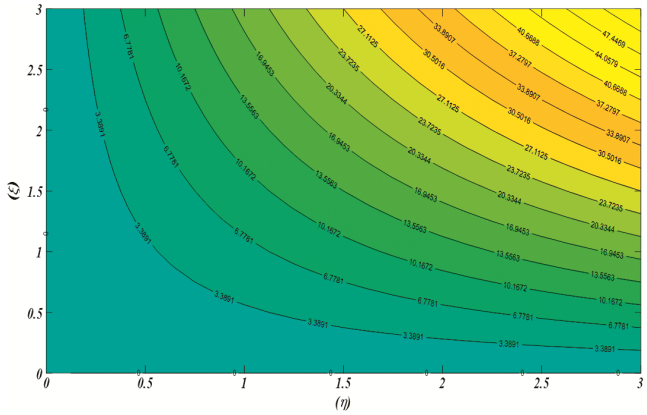

Fig. 27 — Streamlines for increasing ($M = 0.6$) values in ternary hybridity nanofluid.

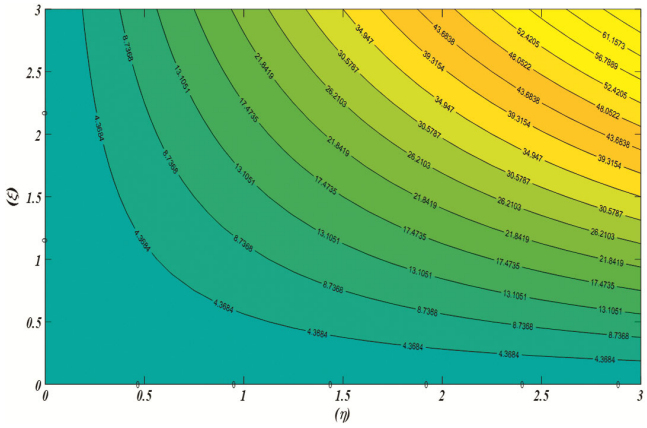

Fig. 28 — Streamlines for increasing ($M = 0.9$)values in ternary hybridity nanofluid.

Newtonian actions, allowing the fluid to shear quicker down the cylinder surface. As the Casson fluid parameter (Ca = 0.5, 1.0, 1.5, 2.0) is raised, the energy transfer rate is seen to decrease a bit.

Figures 37 & 38 show how Newtonian partial slip S_F influence on the cylindrical surfaces shear strain and the regional Nusselt value. In accordance

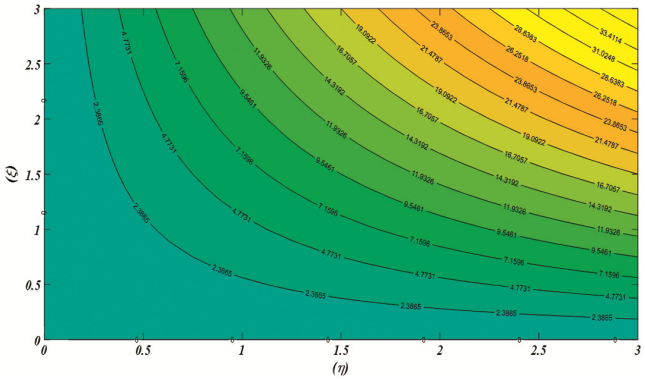

Fig. 29 — Streamlines for increasing ($Ca = 0.0$) values in nanofluid.

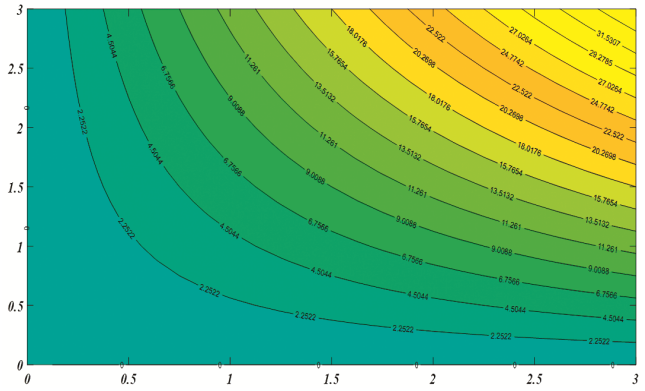

Fig. 30 — Streamlines for increasing ($Ca = 0.3$) values innanofluid.

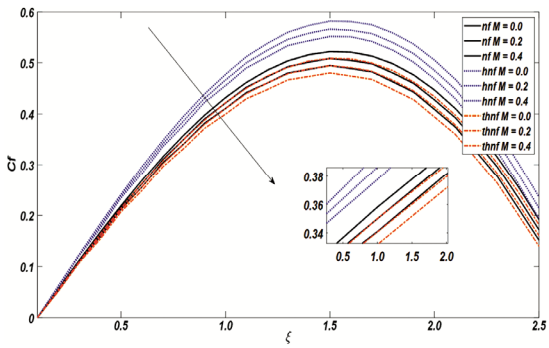

Fig. 31 — The effect of (M) on the C_f.

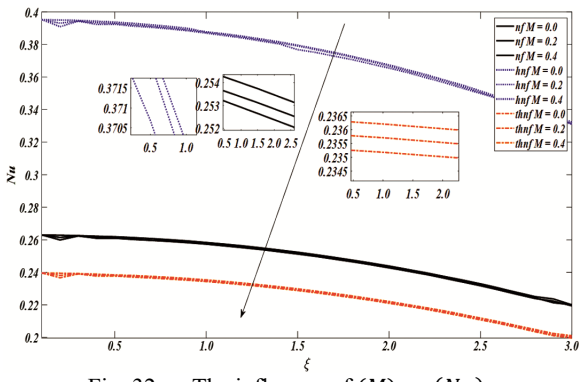

Fig. 32 — The influence of (M) on (Nu).

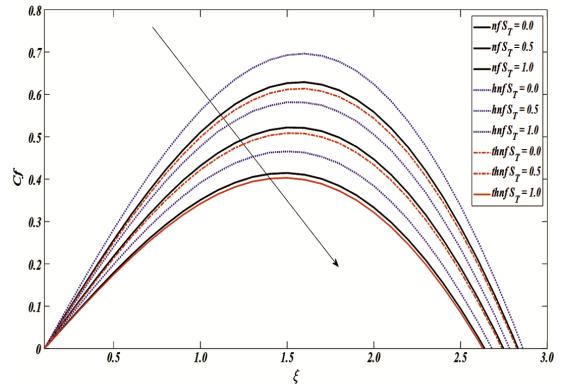

Fig. 33 — The effect of (ST) on C_f.

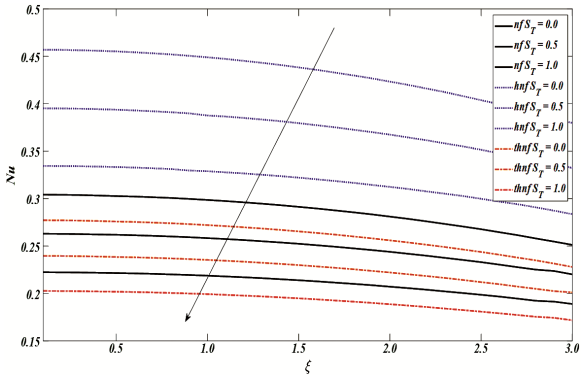

Fig. 34 — The influence of (ST) on (Nu).

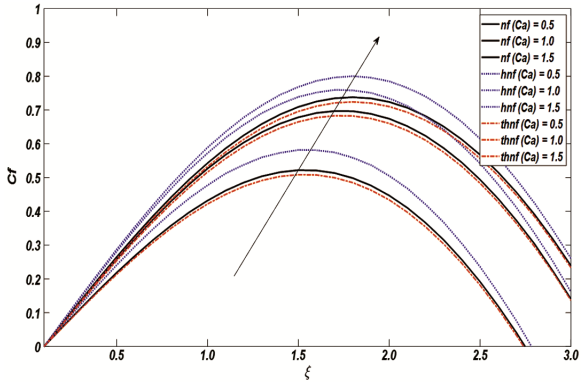

Fig. 35 — The effect of (β) on (C_f).

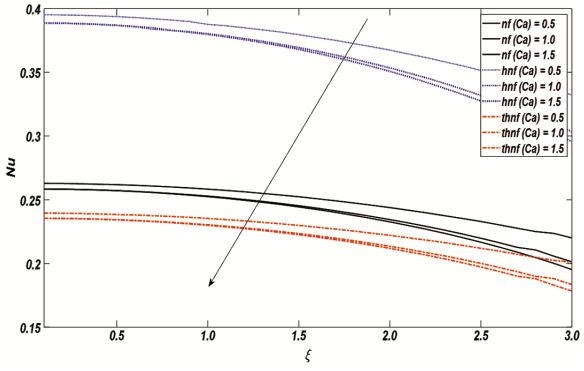

Fig. 36 — The influence of (β) on the (Nu).

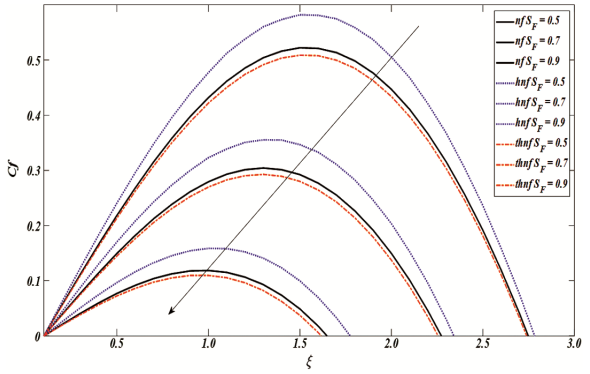

Fig. 37 — The effect of (SF) on (C_f).

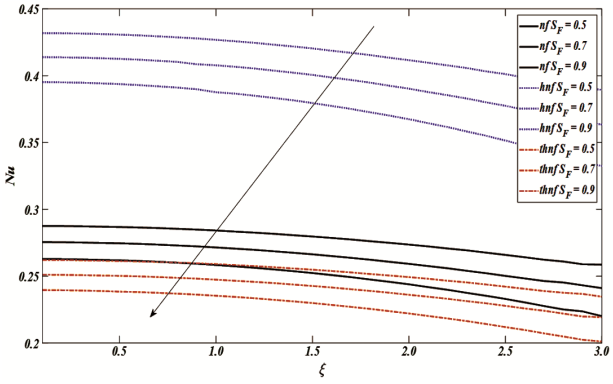

Fig. 38 — The influence of (S_F) on (Nu).

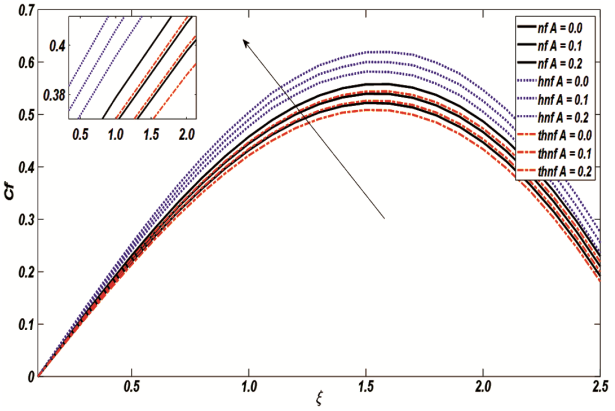

Fig. 39 — The effect of (A) on (C_f).

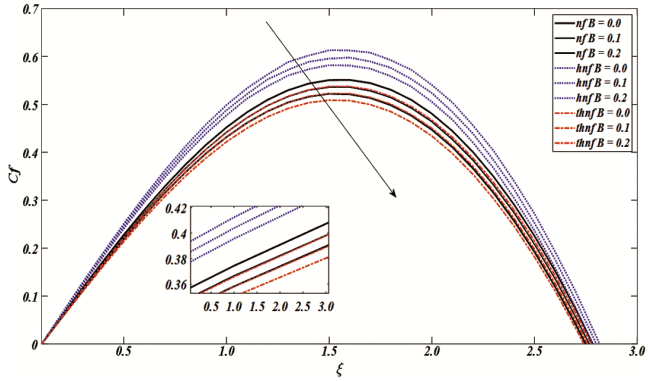

Fig. 40 — The effect of (B) on (C_f).

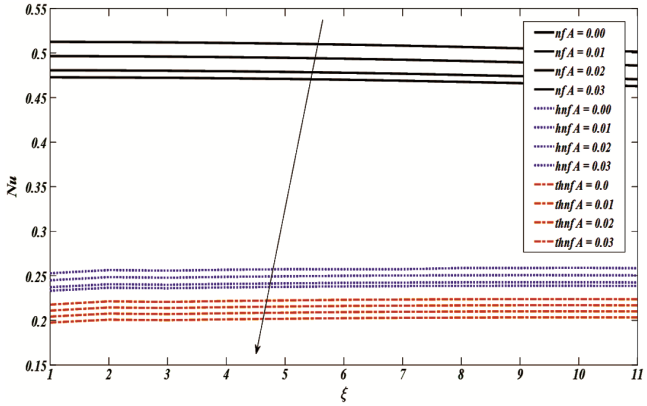

Fig. 41 — The effect of (A) on (Nu).

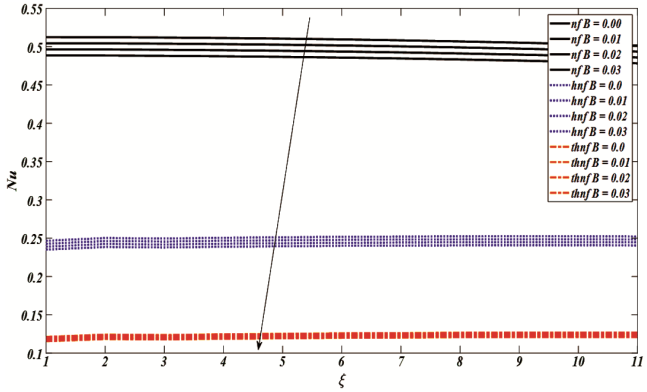

Fig. 42 — The effect of (B) on Nu).

with the prior graphs depicting movement development, increasing $(S_F = 0.5,0.7,0.9)$ steadily decelerates wall shear stress and drops the rate of energy transfer near the cylindrical surface. Figs 39-42 show the impact of irregular heat source (A) and (B) on the skin friction coefficient (Cf). The values of A, increasing the skin friction coefficient also increasing, and the B values increasing the skin friction coefficient is not increasing.

5 Conclusion

The heat transfer properties and flow behaviour of a trihybrid nanofluid $(SiO_2, TiO_2, Al_2O_3, H_2O)$ passing a horizontal circular cylinder are studied. Using appropriate similarity transformations, the governing equations are changed from higher order PDE to first order PDE. The resultant system of differential equations is solved using the (KBM) technique, and the output are graphed. This work may be expanded to investigate the behaviour of other non-Newtonian fluids under various physical conditions by examining the suspension of several classes of nanoparticles that are appropriate for the real scenario.

(1). The hybrid nanoflow transmits more energy for increasing volume fractions.

(2). Titania-silica mixture nanoflow is superior in transferring heat outside from the system.

(3). Raising the velocity of the slip variable(S_f) lowers the movement near the surface of the cylinder as well as the skin friction value, as raising the temperature and decreasing the local Nusselt value.

(4). Raising the value of the Casson fluid parameter raises velocity that the cylinder surface but reduces velocity farther away from the cylinder, as well as fractionally decreasing heat across the boundary zone regime.

(5). Heat transfer rate is for increasing energy generation.

(6). Nusselt number declines as radial coordinate increases for all categories of nanoflow.

(7). Drag coefficient starts with zero and reaches a peak point then it decays to zero as the tangential coordinate rises.

Nomenclature

Dimensional Variables

a	The diameter of the cylinder
g	Gravity-induced acceleration
Gr	Grash of number
α	Diffusivity of heat
Φ	Angular coordinate
ν	Kinematic viscosity
N_0	Factor of velocity slip
K_0	Thermal slip coefficient
Λ	Thermal expansion coefficient
μ	Viscosity in dynamic conditions

Dimensionless Variables

η	Radial coordinate
ξ	Tangential coordinate
ψ	Stream function
u,v	Velocity components in the x and y axes, respectively
f	Stream function
θ	Temperature
S_T	Thermal slip parameter
T	Temperature
S_F	Newtonian slip
Cf	Coefficient of skin friction
$\Pr$	Prandtl number
M	Lorentzian force field
Nu	Nusselt number
Ca	Rheological parameter
A, B	Non-uniform heat source and sink

Suffix w Wall surface

∞ Free flow point

thnf Trihybrid nanoflow
hnf Hybrid nanoflow
nf Nanoflow
f Basefluid

Competing Interests

The authors declare that they have no competing interests.

Acknowledgements

The authors thank the reviewers for their constructive suggestion.

References

1 F Akira & Honda K, *Nature*, 238 (1972) 37.
2 Bischoff B L & Marc A A, *Chem Mater,* 7(1995) 1772.
3 Hulteen J, *J Mater Chem*, 7 (1997) 1075.
4 Zhang, Ming, Bando & Wada K, *J Mater Sci Lett*, 20 (2001) 167.
5 Seo D S, Lee J K & Kim H, *J Crystal Growth*, 229 (2001) 432.
6 Choi S U & Eastman J A, *Enhancing thermal conductivity of fluids with nanoparticles*, 29 (1995).
7 Wang F, Sajid T, Kalbar N M, Jamshed W, Abd-Elmonem & Altamirano G C, *J Comput Des Eng*, (2023) 057.
8 Farooq U, Waqas H, Aldhabani M S, Fatima N, Alhushaybari A A & Muhammad T, *ArabJ Chem*, 16 (2023) 104628.
9 Awwad F A, *Symmetry*, 15 (2023) 1647.
10 Kanafiah S F H M, Kasim A R M, Zokri S M, Arifin & Nordin N S, *CFD Lett*, 15 (2023) 103.
11 Ahmad I, Zan-Ul A Q, Faisal M, Loganathan K, Javed T & Chaudhary D K, *JNanomater*, 2022 (2022).
12 Jamshed W, Eid M R, Al Hossainy A F, Raizah Z, Tag El Din E S M & Sajid T, *Sci Rep*, 12 (2022) 18130.
13 Chandel S, *Hamirpur*, 2023 (2023)].
14 Alwawi F A, Alkasasbeh H T, Rashad A M & Idris R, *J Mech Eng Sci*, 234 (2020) 2569.
15 Kuttan B A, Manjunatha S, Jayanthy S, Gireesha B J & Archana M, *J Nanofluids*, 8 (2019) 845.
16 Abu-Nada E, *Int J Heat Fluid Flow*, 30 (2009) 679.
17 Puneeth V, Manjunatha S, Makinde O D & Gireesha B J, *J Heat Transfer*, 143 (2021) 042502.
18 Sreenivasulu P, Poornima T, Reddy N B & Reddy M G, *J Nanofluids,* 8 (2019) 1076.
19 Sreenivasulu P, Bhaskar Reddy N & Poornima T, *Front Heat Mass Transfer,* 9 (2017).
20 Sreenivasulu P, Poornima T & Reddy PBA, *Mater Sci Eng*, 263 (2017) 062014.
21 Reddy K J, *Multidiscip Model Mater Struct,* 15 (2019) 452.
22 Jyotshna M & Dhanalaxmi V, *Eur J Math Statist*, 3 (2022) 16.
23 Song Y Q, *Alex Eng J*, 61 (2022) 195.
24 Swain K, Parida, Kumar S & Dash G C, *Songklanakarin J Sci Technol*, 44 (2022).
25 Shahzad F, Jamshed W, El Din S M, Shamshuddin M, Ibrahim R W, Raizah Z & Adnan, *Sci Rep*, 12 (2022) 18769.
26 Al Oweidi K F, Shahzad F, Jamshed W, Usman, Ibrahim R W, El Din E S M T & Alderea A M, *Sci Rep*, 12 (2022) 20692.
27 Islam S, Rana B M J, Parvez M S, Hossain M S & Rahman M M, *Int J Thermofluids*, 18 (2023) 100363.
28 Manjunatha S, Puneeth V, Gireesha B J & Chamkha A, *J Appl Comput Mech*, 8 (2022) 1279.
29 Wang Y, Wang Y, Zhang Y, Chai Y, Zhao F & Luo G, *Korean J Chem Eng*, (2023) 1.
30 Sohail M, El-Zahar E R, Mousa A, Nazir U, Althobaiti S, Althobaiti A & Chung J D, *Sci Rep*, 12(2022) 9219.
31 Kalantari D, Tafakhori M, Ghanbari M, Biparva P & Peyghambarzadeh S M, *Int J Therm Sci*, 185 (2023) 108107.
32 Zhao J, Li Z, Zou L, Zhao Y, Tang H, Xu Y & Xiao P, *Vacuum*, 201 (2022) 111120.
33 Prasad V R, Rao A S, Reddy N B, Vasu B & Bég O A, *J Process Mech Eng*, 227 (2013) 309.
34 Cebeci T & Bradshaw P, *Physical and computational aspects of convective heat transfer*, (2012).
35 Puneeth V, Manjunatha S, Makinde O D & Gireesha B J, *J Heat Transfer*, 143 (2021) 042502.